

Communication

Efficient CO₂ Electroreduction over Silver Hollow Fiber Electrode

Shoujie Li^{1,2}, Xiao Dong^{1,3}, Wei Chen^{1,3,*} , Yanfang Song^{1,3}, Guihua Li^{1,3}, Wei Wei^{1,2,3,*} and Yuhan Sun^{1,2,3,*}

¹ CAS Key Laboratory of Low-Carbon Conversion Science and Engineering, Shanghai Advanced Research Institute, Chinese Academy of Sciences, Shanghai 201210, China; lishoujie@sari.ac.cn (S.L.); dongx@sari.ac.cn (X.D.); songyf@sari.ac.cn (Y.S.); liguihua@sari.ac.cn (G.L.)

² School of Physical Science and Technology, ShanghaiTech University, Shanghai 201203, China

³ University of the Chinese Academy of Sciences, Beijing 100049, China

* Correspondence: chenw@sari.ac.cn (W.C.); weiwei@sari.ac.cn (W.W.); sunyh@sari.ac.cn (Y.S.); Tel.: +86-21-20350954 (W.C.); +86-21-20608005 (Y.S.); Fax: +86-21-20350867 (W.C. & Y.S.)

Abstract: Electrocatalytic reduction of CO₂ to fuels and chemicals is one of the most attractive routes for CO₂ utilization. However, low efficiency and poor stability restrict the practical application of most conventional electrocatalysts. Here, a silver hollow fiber electrode is presented as a novel self-supported gas diffusion electrode for efficient and stable CO₂ electroreduction to CO. A CO faradaic efficiency of over 92% at current densities of above 150 mA·cm⁻² is achieved in 0.5 M KHCO₃ for over 100 h, which is comparable to the most outstanding Ag-based electrocatalysts. The electrochemical results suggest the excellent electrocatalytic performance of silver hollow fiber electrode is attributed to the unique pore structures providing abundant active sites and favorable mass transport, which not only suppresses the competitive hydrogen evolution reaction (HER) but also facilitates the CO₂ reduction kinetics.

Keywords: CO₂ electroreduction; silver hollow fiber; gas diffusion electrode; efficient CO formation



Citation: Li, S.; Dong, X.; Chen, W.; Song, Y.; Li, G.; Wei, W.; Sun, Y. Efficient CO₂ Electroreduction over Silver Hollow Fiber Electrode. *Catalysts* **2022**, *12*, 453. <https://doi.org/10.3390/catal12050453>

Academic Editor: Carlo Santoro

Received: 27 March 2022

Accepted: 18 April 2022

Published: 19 April 2022

Publisher's Note: MDPI stays neutral with regard to jurisdictional claims in published maps and institutional affiliations.



Copyright: © 2022 by the authors. Licensee MDPI, Basel, Switzerland. This article is an open access article distributed under the terms and conditions of the Creative Commons Attribution (CC BY) license (<https://creativecommons.org/licenses/by/4.0/>).

1. Introduction

The electroreduction of carbon dioxide (CO₂) to useful chemicals leads to a promising pathway for both CO₂ utilization and the storage of renewable electricity, which is of great significance for achieving carbon neutrality [1,2]. Diverse valuable compounds including syngas, formate [3], methane [4], ethylene [5] and ethanol [6] with a collective market size of over 500 megatonnes per year can be obtained from electrocatalytic CO₂ reduction reaction (eCO₂RR) [7]. Among them, carbon monoxide (CO) as an important component of the commodity syngas (a mixture of CO and H₂) is widely used in the various chemical engineering processes such as Fischer–Tropsch synthesis and methanol synthesis [8,9]. Producing CO on a large scale via CO₂ electrochemical reduction driven by renewable electricity shows an application potential. With respect to the other products such as formic acid (or formate), alcohols and hydrocarbons from CO₂ electroreduction, CO is not only more easy to separate from the aqueous electrolyte solution, but also efficiently generated with fewer electrons (two-electron transfer) at slight negative potentials [10]. Therefore, there have been many efforts focusing on electrocatalyst development to achieve highly efficient CO₂ conversion to CO [7,10–15].

Among various materials that have been studied as electrocatalysts, silver (Ag) is a promising material that possesses the efficient capability to electroreduce CO₂ into CO and also costs much less than other precious metal catalysts [16,17]. Its all-inorganic nature would be more stable than homogeneous catalysts [18,19]. Although faradaic efficiency (FE) of up to 90% for eCO₂RR towards CO has been achieved over various Ag-based catalysts, such as OD-Ag [20], BD-Ag [21], POD-Ag [22], P-Ag [23] and AE-Ag [24], in an aqueous H-cell type electrolyzer, the current densities of these catalysts are generally

below $10 \text{ mA}\cdot\text{cm}^{-2}$ for eCO_2RR to CO. Moreover, even though higher current densities could be achieved through electrode nanostructuring [19,25], the current densities were still limited to below $30 \text{ mA}\cdot\text{cm}^{-2}$ [26,27] due to the low aqueous solubility of CO_2 and long diffusion distance in the electrolyte, failing to reach the $>100 \text{ mA}\cdot\text{cm}^{-2}$ regime needed to make eCO_2RR electroreduction to CO economically viable [28,29].

Recently, gas-diffusion electrodes (GDEs) have been adopted to allow sufficient CO_2 supply and enhance triple-phase interface reactions between CO_2 , catalyst and electrolyte [26,29–32]. By using an ionomer layer with hydrophobic and hydrophilic functionalities, the reaction interface is increased from the submicrometer regime to the several-micrometer-length scale in the GDEs [31]. Current densities of up to hundreds of milliamperes per square centimeter have been achieved with alkaline electrolyte [32]. However, these GDEs are prone to flooding due to electro-wetting under cathodic conditions or carbonation-derived pore blockage as the result of the reaction between CO_2 and alkaline electrolytes, encumbering performance stability [33]. In addition, the multiple components and complicated structures hinder the practical applications of the GDEs. In contrast, the hollow fiber (HF) electrode is a kind of novel self-supported gas-diffusion electrode that can be used as both a working electrode and a gas diffuser. Its tubular shape and porous hierarchical walls result in a compulsory gas flow-through configuration and abundant three-phase reaction interfaces [34,35]. For example, Cu HF electrodes have been employed for eCO_2RR to CO, with an order of magnitude higher current density achieved compared with nanocrystalline Cu electrodes due to such favorable mass transport conditions [34]. Although higher current densities have been achieved through further optimization [35–37], to date, most of these HF electrodes still deliver limited selectivity ($\text{FE}_{\text{eCO}_2\text{RR}} \leq 90\%$) for efficient CO_2 electrochemical conversion.

Here, we adopted a silver hollow fiber (Ag HF) electrode composed of only metallic Ag for the electroreduction of CO_2 to CO. The fused Ag particles in Ag HF not only build it to be a tough self-supported gas-diffusion electrode without any binder, but also induce the promotion of eCO_2RR while the competitive HER is suppressed. Notably, a CO faradaic efficiency over 92% at current densities above $150 \text{ mA}\cdot\text{cm}^{-2}$ in 0.5 M KHCO_3 with a 100 h sustained performance was achieved, which is comparable to reported excellent Ag-based electrocatalysts (Table S2).

2. Results

The Ag HF was fabricated by a combined phase inversion/sintering process from commercial Ag powder (Figure S1, see Section 4 for details). Figure 1A shows the slender Ag HF tubes with a metallic luster. Typical cross-sectional scanning electron microscope (SEM) images showed a uniform wall thickness of $\sim 40 \mu\text{m}$ and an outer diameter of $\sim 400 \mu\text{m}$ for the Ag HF (Figure 1B,C). No initial spherical Ag particles (Figure S2) were discerned from the SEMs of Ag HF, implying that a well-fused porous substrate was constructed by sintering (Figures 1D and S3). Moreover, the interconnected microporous channels formed by particle fusion (Figures 1E and S3) are conducive to the efficient transportation of CO_2 to the three-phase reaction interface to ensure sufficient CO_2 supply for electroreduction [34,37]. On the other hand, these microstructures may provide low-coordination sites such as edges and corners with higher density, which could bind more strongly with adatoms than flat surfaces, and also could possess a high electric field due to their high curvature [34,35].

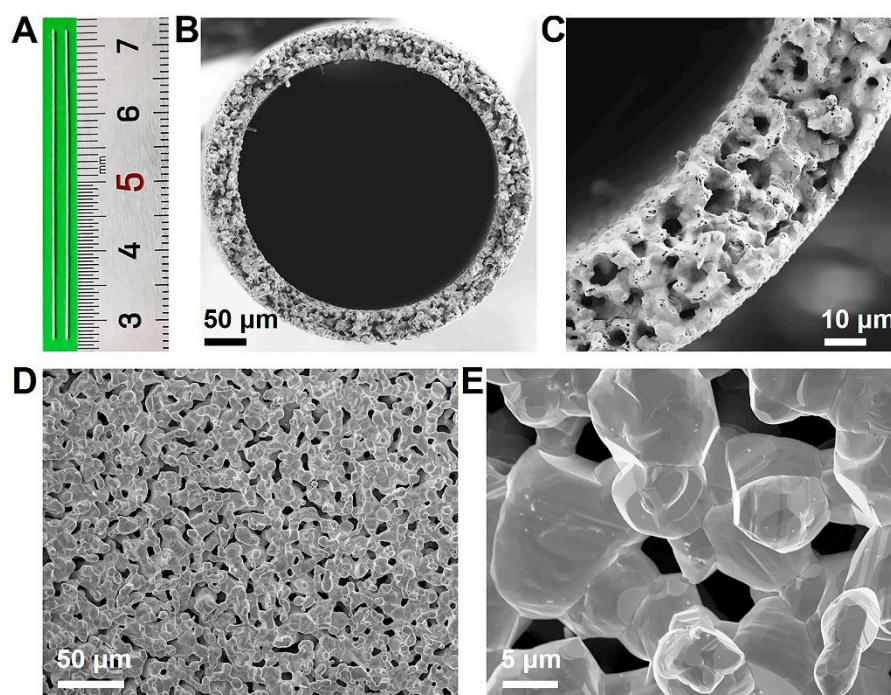


Figure 1. Characterization of Ag HF: (A) optical image and SEM images of (B,C) cross-sections and (D,E) outer surfaces of Ag HF.

The X-ray diffraction (XRD) pattern (Figure S4) of Ag HF showed peaks at 38.1, 44.3, 64.4, 77.5 and 81.5°, the same as those of commercial Ag powder and Ag foil, which should be assigned to the (111), (200), (220), (311) and (222) planes of metallic Ag (JCPDS No. 04–0783), respectively. High-resolution transmission electron microscopy (HRTEM) also showed that the Ag HF and Ag foil are composed of metallic Ag, with the d-spacing of 2.36 Å which corresponds to the lattice fringe of Ag (111) (Figure S5), consistent with the XRD results. Moreover, X-ray photoelectron spectroscopy (XPS) of Ag 3d spectra (Figure S6) for Ag HF showed Ag 3d_{5/2} and Ag 3d_{3/2} peaks at binding energies of 368.2 and 374.2 eV, respectively, indicating the metallic Ag⁰ characteristics of the sample surface, which is identical to commercial Ag powder and Ag foil. These results verified that both the bulk and surface compositions of Ag HF are completely identical to those of Ag powder and Ag foil as metallic Ag⁰.

All mentioned electrochemical experiments with the Ag HF electrode as both the working electrode and gas diffuser were conducted in CO₂-saturated KHCO₃ solution (Figure S7, see Section 4 for details). In this work, a flow rate of 30 mL·min^{−1} of CO₂ was chosen to ensure that the reaction is not limited by a lack of CO₂ supply and to compare our performance with other studies [34,36]. As shown in Figure 2A, only CO and H₂ were detected over the Ag HF electrode with a total faradaic efficiency (FE) of ~100% in the potential range of −0.7 to −1.4 V. Note that the generation of H₂ was well suppressed within the whole potential range (−0.7 to −1.4 V), consistently resulting in CO FEs greater than 80%. The exclusive formation of CO for eCO₂RR led to a CO FE greater than 90%, especially at −0.9 to −1.3 V. In addition, the corresponding current densities (*j*) of eCO₂RR products showed the same trend (Figure 2B). Both total current densities and CO partial current densities (*j*_{CO}) increased rapidly at more negative potentials, while the H₂ partial current densities (*j*_{H₂}) increased slowly, giving a ~141 mA·cm^{−2} *j*_{CO} with a CO FE as high as 92.7% at −1.2 V. The corresponding CO formation rate, cathodic energy consumption, outlet CO concentration and CO energy efficiency of Ag HF were 2636.8 μmol·h^{−1}·cm^{−2}, 91.5 mW·cm^{−2}, 1.79% and 51.1%, respectively (Table S1), comparable to those of other prominent electrocatalysts [31,35,38]. The CO FEs of Ag foil were lower than 60% in all potentials, giving the largest CO FE of ~56% at −0.9 V with a lower 5 mA·cm^{−2} *j*_{CO}

(Figure S8). In contrast, the j_{CO} of Ag HF reached as high as $194 \text{ mA}\cdot\text{cm}^{-2}$ at -1.4 V , which is about 42 times that for Ag foil ($4.6 \text{ mA}\cdot\text{cm}^{-2}$), evidencing the striking promotion in the intrinsic activity of Ag.

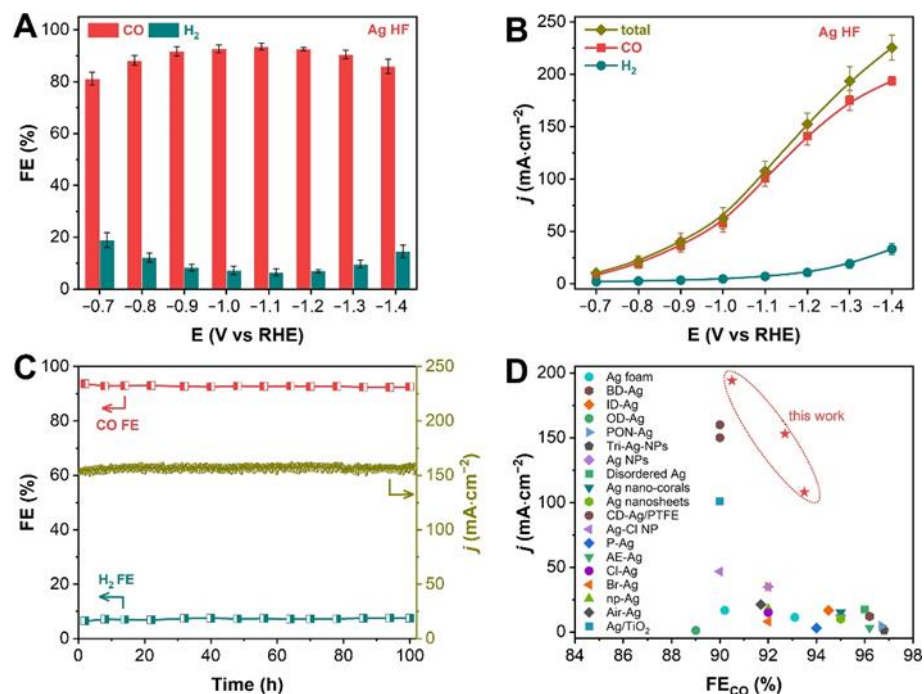


Figure 2. The eCO₂RR performance of Ag HF. (A) CO and H₂ faradaic efficiencies and (B) current densities of eCO₂RR over Ag HF in the potential range of -0.7 to -1.4 V . (C) Long-term performance of Ag HF at -1.2 V . (D) Performance comparison of Ag HF with recently reported outstanding Ag-based electrocatalysts for CO₂ electroreduction to CO (details in Table S2).

The long-term performance of electrocatalysts is of great importance for their practical applications [26]. Although many studies [20–25] have reported that Ag-based electrocatalysts possess the capability to selectively electroreduce CO₂ into CO, most of their current densities for long-term tests are restricted below $100 \text{ mA}\cdot\text{cm}^{-2}$ (Figure 2C and Table S2). On the other hand, although relatively higher current densities have been achieved through GDEs in highly alkaline electrolytes, the use of basic media poses significant stability challenges [27,32]. For example, the carbon-based GDE was found to degrade over 2 h in a basic electrolyte during eCO₂RR [38]. In sharp contrast, the durability of a Ag HF electrode was evaluated in a continuous CO₂ electrolysis test operated at -1.2 V with 0.5 M KHCO_3 . As shown in Figure 2C, the CO FE remained between 92% and 93% with a fluctuating total current density of 150 – $160 \text{ mA}\cdot\text{cm}^{-2}$. No sign of decline was observed during the 100 h test. Such excellent long-term performance is comparable to that of excellent Ag-based GDEs in a flow cell system and much higher than that of outstanding Ag-based electrocatalysts in an aqueous H-cell electrolyzer (Figure 2D and Table S2) [11,19–25,32,39–47]. The postreaction XRD and XPS (Figure S9) revealed the stable compositions of Ag HF after electrolysis, which were responsible for the steady CO₂ electroreduction performance, providing great prospects for scalable eCO₂RR applications.

The electrochemically active surface areas (ECSAs) of Ag HF and Ag foil were examined by measuring their double-layer capacitance (C_{dl}) values from their cyclic voltammetry curves (Figures 3A and S10). The resulting ECSAs were 6.0 and $1.9 \text{ mF}\cdot\text{cm}^{-2}$ for Ag HF and Ag foil, respectively. Note that the ECSA value for Ag HF is 3.2 times that for Ag foil, far away from the disparity in j_{CO} (38 times) (Figures 2B and S11) at the same potential (-1.2 V). Then, we normalized the j_{CO} and j_{H_2} by their ECSAs (Figure S12). The results showed that the j_{CO} of Ag HF was always much higher than that of Ag foil at the same

potentials regardless of whether it was normalized or not (Figures 2B, S11A and S12A). In addition, even though the j_{H_2} plot showed that the Ag HF had a similar j_{H_2} to the Ag foil (Figure S11B), the normalized j_{H_2} of the Ag HF was much lower than that of the Ag foil at the same potentials (Figure S12B). These results implied that the high value of ECSA may only play a partial role in the efficient formation of CO over the Ag HF electrode [35]. The intrinsic activity of the Ag HF may largely be promoted by its unique structure, facilitating the eCO₂RR while the HER was suppressed.

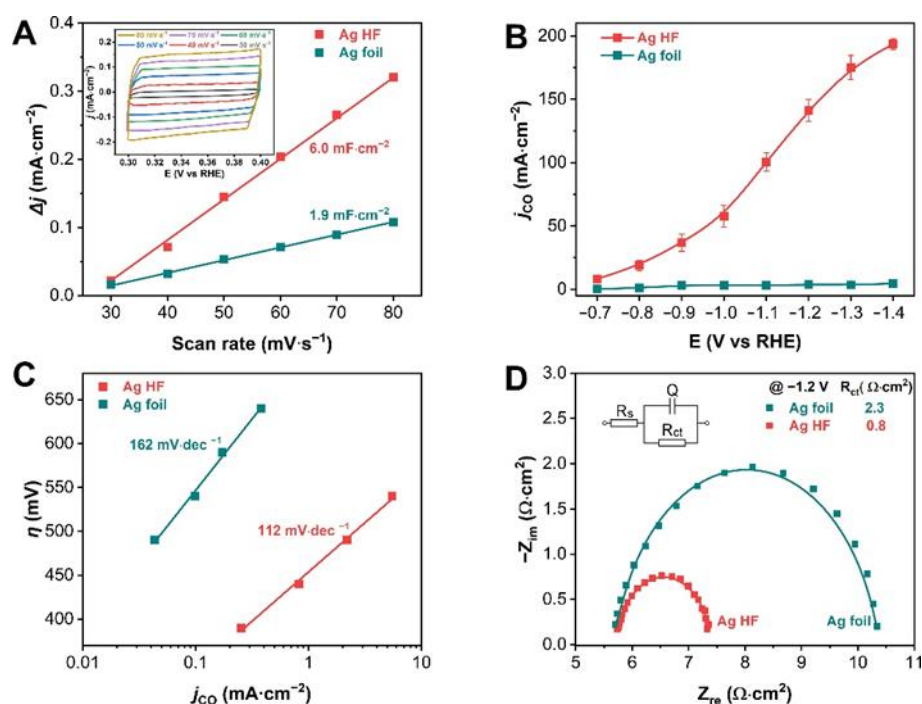


Figure 3. Electrochemical characterization. (A) Plot of Δj (the difference of cathodic and anodic current densities, $j_c - j_a$) against the scan rates of cyclic voltammetry curves (Figure S10); (B) CO partial current density comparison (Figure S11) (C); Tafel slopes; (D) EIS Nyquist plots of Ag HF and Ag foil. The inset in D shows the equivalent circuit.

Then, a Tafel analysis was further performed to gain insight into the underlying kinetic mechanism for the eCO₂RR over the Ag HF (Figure 3C). The Tafel slopes of both Ag foil ($162 \text{ mV} \cdot \text{dec}^{-1}$) and Ag HF ($112 \text{ mV} \cdot \text{dec}^{-1}$) were close to $118 \text{ mV} \cdot \text{dec}^{-1}$, which is the commonly suggested Tafel slope when the rate-determining step for eCO₂RR is the initial electron transfer to CO₂ to form a surface-adsorbed $^* \text{COO}^-$ intermediate [12,48] (step 1 of Figure S13). Note that the Tafel slope of Ag HF was much lower than that of Ag foil, implying a faster initial electron transfer to a CO₂ molecule for CO₂ activation [49], which may improve the intrinsic catalytic activity of Ag HF towards CO formation. Such a faster electron transfer was also verified by the lower interfacial charge transfer resistance (R_{ct}) of Ag HF ($0.8 \Omega \cdot \text{cm}^2$) compared with that of Ag foil ($2.3 \Omega \cdot \text{cm}^2$), as shown in Figure 3D. The improved charge transfer indicates that faster electrochemical reduction occurs on the Ag HF [37], and this is in accordance with the eCO₂RR performance results shown in Figure 3B. Consequently, these results suggested that the improved initial one-electron transfer enhanced the intrinsic CO₂ reduction activity over the Ag HF, resulting in such high activity for the electrocatalytic reduction of CO₂ to CO.

3. Discussion

Besides the improved initial one-electron transfer and the higher-ECSA-enhanced intrinsic CO₂ reduction activity of Ag HF, the high activity and selectivity for the electrocatalytic reduction of CO₂ to CO might also be associated with the favorable mass transfer

and abundant three-phase reaction interfaces of the Ag HF due to its compulsory gas flow-through configuration [34]. The CO₂ molecules are forced to penetrate through the porous wall of the Ag HF electrode, resulting in compulsive interaction of CO₂ with the reaction active sites and further effective activation, which synergistically facilitates CO formation [34,35]. On the other hand, the hollow fiber configuration of the Ag HF electrode might also be beneficial for the removal of CO from the electrode surface, induced by the very high local concentration of CO₂ near the electrode surface, which might boost the CO production rate over the Ag HF [34].

Compared with the conventional GDEs with multiple components, the Ag HF exhibits the following striking merits: (1) It is formed from a single component. High-purity commercial silver powder was subjected to the combined phase inversion/sintering process to obtain the Ag HF without any additive binder. (2) It has a tough and integral substrate. Due to the sintering step, the Ag particles in Ag HF are fused, indicating the formation of a tough and integral substrate, which not only exhibits structural stability but also facilitates electron transport. (3) It has tunable pore structures. The pore structures of Ag HF can be further improved via the optimized preparation procedures to promote CO₂ supply and dispersion, resulting in enhanced CO₂ electroreduction performance.

As a matter of fact, although the Ag HF we reported here could efficiently and stably electroreduce CO₂ to CO by virtue of abundant active sites and favorable mass transport due to its unique pore structures, the $\leq 300 \text{ mA}\cdot\text{cm}^{-2}$ current densities are still limitations to affording an economically viable CO₂ electrochemical conversion [26,30]. Future studies could be aimed at the optimization of hollow fiber configurations, such as tuning the surface morphology and size of Ag nanoparticles to obtain more active sites through synthesizing nanostructured [50] or oxide-derived Ag catalysts [20] to give full play to the improved favorable mass transport of the Ag HF for more efficient CO₂ electroreduction for scalable applications.

4. Materials and Methods

4.1. Materials

Ag powder (99.9%, 50 nm) was purchased from Ningbo Jinlei Nano Materials Co., Ltd. (Ningbo, China). Ag foil (99.9%, 1 mm thick) was purchased from Shanghai Macklin Biochemical Technology Co., Ltd. (Shanghai, China). Polyetherimide (PEI) was purchased from Saudi Basic Industries Corporation (SABIC) (Guangdong, China). N-Methyl-2-pyrrolidone (NMP) and potassium bicarbonate (KHCO₃) were purchased from Sinopharm Chemical Reagent Co., Ltd. (Shanghai, China). Nafion 117 proton exchange membranes (PEM) were purchased from DuPont (Shanghai, China). 3-Trimethylsilyl-1-propane sulfonic acid sodium salt (DSS) was purchased from Sigma-Aldrich (Shanghai, China). All chemicals were used as received without further purification. Electrolyte solutions were prepared using 18.2 MΩ H₂O (ultrapure water, from Master-S30UVF water purification system).

4.2. Catalyst Preparation

The Ag HF was fabricated by a combined phase-inversion/sintering process (Figure S1). Briefly, commercially available polyetherimide (PEI, 24 g) was added to N-methyl-2-pyrrolidone (NMP, 96 g), followed by ultrasonic treatment for 1 h to obtain a homogeneous and transparent solution. Then, Ag powder (80 g) was added to the above solution. The as-obtained mixture was further treated by ball-milling (300 rpm) for 24 h to form a uniform slurry. After cooling to room temperature, the slurry was vacuumized (1 mbar) for 5 h to remove bubbles to obtain a casting solution. Next, the casting solution was extruded through a spinning machine and shaped in a water bath via the phase-inversion process. After spinning, the as-formed tubes were kept in a water bath for 24 h to eliminate the solvent completely, followed by stretching and drying for 48 h to obtain a green body. The green body was cut into appropriate lengths and then calcinated in an air flow (100 mL·min⁻¹) at 600 °C (heating rate: 1 °C·min⁻¹) for 6 h to remove PEI. After being naturally cooled to

room temperature, the calcined green body was then reduced in a 5% H₂ (argon balance) flow (100 mL·min⁻¹) at 300 °C (heating rate: 1 °C·min⁻¹) for 3 h to obtain Ag HF.

The Ag HF with an exposed length of 4 cm was stuck into a copper tube using conductive silver adhesive for electrical contact, while the end of the Ag HF tube as well as the joint between the Ag HF and copper tube were sealed and covered with gas-tight and nonconductive epoxy. After drying at room temperature for 24 h, a Ag HF electrode was obtained with an exposed geometric area of 0.5 cm² ($S = \pi DL = 3.14 \times 400 \times 10^{-4} \times 4 = 0.5 \text{ cm}^2$) and a silver loading of $14 \pm 1 \text{ mg}\cdot\text{cm}^{-2}$.

A piece of Ag foil was ultrasonically cleaned in acetone and ethanol, and after drying in air, the side and back of the Ag foil were sealed with epoxy to obtain a Ag foil electrode with an exposure geometric area of 1 cm × 0.5 cm and a silver loading of $1000 \pm 50 \text{ mg}\cdot\text{cm}^{-2}$.

4.3. Catalyst Characterization

The cross-section and surface morphologies of Ag HF were observed via scanning electron microscopy (SEM) using a Supra 55 microscope with an accelerating voltage of 5.0 kV. Transmission electron microscopy (TEM) investigations were conducted with a JEM-ARM300F microscope operated at 300 kV. X-ray diffraction (XRD) measurements were performed on a Rigaku Ultima 4 X-ray diffractometer using a Cu K α radiation source ($\lambda = 1.54056 \text{ \AA}$) at 40 kV and 40 mA. X-ray photoelectron spectroscopy (XPS) tests were conducted using a Quantum 2000 Scanning ESCA Microprobe instrument with a monochromatic Al K α source (1486.6 eV). The binding energies in all XPS spectra were calibrated according to the C 1s peak (284.8 eV).

4.4. Electrochemical Measurements

Electrochemical characterization was performed on a Biologic VMP3 potentiostat (Bio-Logic Inc., Seyssinet-Pariset, France) in a two-compartment electrolysis cell with a three-electrode configuration at room temperature. The Ag HF electrode was used as the working electrode, with a KCl-saturated Ag/AgCl reference electrode in the cathodic compartment and a platinum mesh counter electrode in the anodic compartment (Figure S7). The electrochemically active surface area (ECSA) of the electrode was evaluated by the double-layer capacitance (C_{dl}). The C_{dl} was determined by performing cyclic voltammetry (CV) in the potential range of 0.4 to 0.5 V (vs. RHE) at different scan rates in CO₂-saturated 0.5 M KHCO₃. The electrochemical impedance spectroscopy (EIS) measurements were performed in CO₂-saturated 0.5 M KHCO₃ at -1.2 V (vs. RHE), and the frequency limits were typically set in the range of 0.1 Hz to 100 kHz with a voltage amplitude of 50 mV. Prior to the experiments, the electrolysis cell was vacuumized and then purged with high-purity CO₂ (99.999%, Shanghai Pujiang Special Gas Corp., Shanghai, China) for 30 min, after which CO₂ was continuously delivered into the cathodic compartment at a constant rate of 30 mL·min⁻¹. All the applied potentials were recorded against the KCl-saturated Ag/AgCl reference electrode and then converted to those versus the reversible hydrogen electrode (RHE) with iR corrections by the following equation:

$$E(\text{vs. RHE}) = E(\text{vs. Ag/AgCl}) + 0.197V + 0.0591V \times pH + 0.85iR_s$$

where E (vs. Ag/AgCl) is the applied potential, pH is the pondus hydrogenii value of the electrolyte solutions (~ 7.2 , CO₂-saturated 0.5 M KHCO₃), i is the current density at each applied potential, and R_s is the solution resistance obtained by EIS measurements ($\sim 5.7 \Omega\cdot\text{cm}^2$). All applied potentials in the main text and Supplementary Materials refer to the RHE unless otherwise stated.

During the stability test of Ag HF CO₂ electroreduction, the potential was fixed at -1.2 V (vs. RHE), the electrolyte was CO₂-saturated 0.5 M KHCO₃ and the CO₂ flow rate was kept at 30 mL·min⁻¹. The catholyte and anolyte were cycled at a flow rate of 10 mL·min⁻¹ by using two identical peristaltic pumps (Jihpump BT-50EA 153YX), accompanied by the supplement of ultrapure water to maintain a constant concentration of 0.5 M KHCO₃. In addition, the postreaction catholyte and anolyte were subjected to

inductively coupled plasma element measurements, and no dissolved silver or platinum ions were found.

4.5. Product Quantifications

Gas-phase products from the cathodic compartment were directly vented into a gas chromatograph (GC-2014, Shimadzu Co., Ltd., Kyoto, Japan) equipped with a Shincarbon ST80/100 column and a Porapak-Q80/100 column with a flame ionization detector (FID) and a thermal conductivity detector (TCD) during the electroreduction tests and analyzed online. The FID detector was used for CO quantification (as well as CH₄, C₂H₄ and C₂H₆), while TCD was used for H₂ quantification. All faradaic efficiencies reported were based on at least three different GC runs. High-purity argon (99.999%) was used as the GC carrier gas. In all the CO₂ electrolysis tests, only H₂ and CO were the gas-phase products, and their faradaic efficiencies were calculated as follows:

$$FE = \frac{C_{product} \times 10^{-6} \times v_{CO_2} \times 10^{-3} \times t \times \alpha \times F}{V_m \times Q} \times 100\%$$

where $C_{product}$ is the concentration of the gas-phase products (ppm), v_{CO_2} is the flow rate of CO₂ (30 mL·min⁻¹), t is the reaction time, α is the number of transferred electrons for producing CO or H₂, F is the Faraday constant, V_m is the gas mole volume and Q is the total quantity of the electric charge. The CO formation rate was calculated using the following equation:

$$CO \text{ formation rate} = \frac{Q \times FE_{CO}}{F \times n \times t \times S}$$

where S is the geometric area of the electrode (cm²). The cathodic energy consumption was calculated as follows:

$$p_{cathodic} = E \times i$$

where E is the applied potential vs. RHE after iR compensation. By assuming that the overpotential of oxygen evolution reaction on the anode side is zero, the cathodic energy efficiency for CO was calculated as follows [38]:

$$EE_{CO} = \frac{(1.23 + (-E_{CO})) \times FE_{CO}}{1.23 + (-E)}$$

where E_{CO} is -0.11 V (vs. RHE); 1.23 V is the thermodynamic potential for water oxidation on the anode side.

Possible liquid-phase products from the cathodic compartment after CO₂ electrolysis for 1 h were analyzed using another off-line GC-2014 (Shimadzu Co., Ltd., Kyoto, Japan) equipped with a headspace injector and an OVI-G43 capillary column (Supelco[®], Sigma-Aldrich Inc., St. Louis, MO, USA). No liquid-phase products were detected by the off-line GC. The postreaction catholyte solution was also analyzed by a 600 MHz NMR spectrometer (Bruker, Karlsruhe, Germany) for possible liquid-phase products, especially formate and acetate. After an hour of electrolysis, an aliquot of catholyte solution (0.5 mL) was mixed with 0.1 mL DSS (6 mM) as internal standard and 0.1 mL D₂O. No liquid-phase product was detected by NMR.

5. Conclusions

In this work, we report a three-dimensional silver hollow fiber electrode used as both a working electrode and a gas diffuser for highly efficient and stable electroreduction of CO₂ to CO. A CO faradaic efficiency of over 92% at current densities of above 150 mA·cm⁻² with a 100 h sustained performance was achieved in 0.5 M KHCO₃, which is comparable to the most outstanding Ag-based electrocatalysts. The experimental results suggested that the excellent electrocatalytic performance of the electrode is attributed to the unique pore structures, providing abundant active sites in addition to favorable mass transport,

which not only suppressed the competitive HER but also facilitated the CO₂ reduction. In addition, the Ag HF may become an ideal industrial electrode due to its tough framework and mature preparation process, showing great potential for scalable applications.

Supplementary Materials: The following are available online at <https://www.mdpi.com/article/10.3390/catal12050453/s1>, Figure S1. Schematic illustration showing the general procedures for the fabrication of the Ag HF. Figure S2: SEM image of commercially available silver powder; Figure S3: SEM images of the (A,B) outer and (C,D) inner surfaces of the Ag HF. Figure S4: XRD patterns of Ag foil, Ag powder and Ag HF. Figure S5: TEM images of (A) Ag foil and (B) Ag HF. Figure S6: XPS spectra of Ag foil, Ag powder and Ag HF. Figure S7: Schematic illustration of porous silver hollow fiber for efficient CO production via eCO₂RR. Figure S8: (A) CO and H₂ faradaic efficiencies and (B) current densities of eCO₂RR over Ag foil in the potential range from −0.7 to −1.4 V. Figure S9: (A) XRD patterns and (B) XPS spectra of Ag foil and Ag HF before and after eCO₂RR. Figure S10: Cyclic voltammety curves of (A) Ag foil and (B) Ag HF in 0.5 M KHCO₃. (C) Plot of Δj (the difference of cathodic and anodic current densities, $j_c - j_a$) against the scan rates from cyclic voltammety curves. The plots in Figure S10C are the same as those in Figure 3A in the main text. Figure S11: (A) CO and (B) H₂ partial current densities over Ag foil and Ag HF in the potential range of −0.7 to −1.4 V. Figure S12: (A) ECSA-normalized CO and (B) H₂ partial current densities over Ag foil and Ag HF in the potential range of −0.7 to −1.4 V. Figure S13: Proposed reaction steps for the electroreduction of CO₂ to CO on silver catalysts. Table S1: Detailed eCO₂RR performances of the Ag HF electrode. Table S2: Electrocatalytic performances for CO₂ to CO over typical recently reported Ag-based catalysts.

Author Contributions: Conceptualization, W.C.; investigation, S.L.; data curation, S.L.; writing—original draft preparation, S.L.; writing—review and editing, W.C., X.D., Y.S. (Yangfang Song), G.L., W.W. and Y.S. (Yuhan Sun); supervision, W.C. and W.W.; funding acquisition, W.C. and Y.S. (Yangfang Song). All authors have read and agreed to the published version of the manuscript.

Funding: This research was funded by the National Natural Science Foundation of China (Nos. 91745114 and 21802160), the “Transformational Technologies for Clean Energy and Demonstration” Strategic Priority Research Program of the Chinese Academy of Sciences (No. XDA 21000000), the Hundred Talents Program of the Chinese Academy of Sciences (No. 2060299), the Shanghai Sailing Program (No. 18YF1425700), the Shanghai Functional Platform for Innovation Low Carbon Technology and the Major Project of the Science and Technology Department of Inner Mongolia (No. 2021ZD0020).

Institutional Review Board Statement: Not applicable.

Informed Consent Statement: Not applicable.

Data Availability Statement: Not applicable.

Acknowledgments: Financial support from the National Natural Science Foundation of China (Nos. 91745114 and 21802160), the “Transformational Technologies for Clean Energy and Demonstration” Strategic Priority Research Program of the Chinese Academy of Sciences (No. XDA 21000000), the Hundred Talents Program of the Chinese Academy of Sciences (No. 2060299), the Shanghai Sailing Program (No. 18YF1425700), the Shanghai Functional Platform for Innovation Low Carbon Technology and the Major Project of the Science and Technology department of Inner Mongolia (No. 2021ZD0020) is gratefully acknowledged.

Conflicts of Interest: The authors declare no conflict of interest.

References

1. Chu, S.; Majumdar, A. Opportunities and challenges for a sustainable energy future. *Nature* **2012**, *488*, 294–303. [[CrossRef](#)] [[PubMed](#)]
2. Davis, S.J.; Caldeira, K.; Matthews, H.D. Future CO₂ emissions and climate change from existing energy infrastructure. *Science* **2010**, *329*, 1330–1333. [[CrossRef](#)] [[PubMed](#)]
3. Díaz-Sainz, G.; Alvarez-Guerra, M.; Irabien, A. Continuous electroreduction of CO₂ towards formate in gas-phase operation at high current densities with an anion exchange membrane. *J. CO₂ Util.* **2022**, *56*, 101822. [[CrossRef](#)]
4. Xue, L.; Zhang, C.; Wu, J.; Fan, Q.-Y.; Liu, Y.; Wu, Y.; Li, J.; Zhang, H.; Liu, F.; Zeng, S. Unveiling the reaction pathway on Cu/CeO₂ catalyst for electrocatalytic CO₂ reduction to CH₄. *Appl. Catal. B-Environ.* **2022**, *304*, 120951. [[CrossRef](#)]

5. Kuo, L.; Dinh, C.T. Toward efficient catalysts for electrochemical CO₂ conversion to C₂ products. *Curr. Opin. Electrochem.* **2021**, *30*, 100807. [[CrossRef](#)]
6. Cheng, D.; Zhao, Z.-J.; Zhang, G.; Yang, P.; Li, L.; Gao, H.; Liu, S.; Chang, X.; Chen, S.; Wang, T.; et al. The nature of active sites for carbon dioxide electroreduction over oxide-derived copper catalysts. *Nat. Commun.* **2021**, *12*, 395. [[CrossRef](#)]
7. Tang, M.T.; Peng, H.; Lamoureux, P.S.; Bajdich, M.; Abild-Pedersen, F. From electricity to fuels: Descriptors for C1 selectivity in electrochemical CO₂ reduction. *Appl. Catal. B-Environ.* **2020**, *279*, 119384. [[CrossRef](#)]
8. Hernandez, S.; Farkhondehfar, M.A.; Sastre, F.; Makkee, M.; Saracco, G.; Russo, N. Syngas production from electrochemical reduction of CO₂: Current status and prospective implementation. *Green Chem.* **2017**, *19*, 2326–2346. [[CrossRef](#)]
9. Verma, S.; Kim, B.; Jhong, H.; Ma, S.C.; Kenis, P.J.A. A gross-margin model for defining techno-economic benchmarks in the electroreduction of CO₂. *ChemSusChem* **2016**, *9*, 1972–1979. [[CrossRef](#)]
10. Ren, S.X.; Joulie, D.; Salvatore, D.; Torbensen, K.; Wang, M.; Robert, M.; Berlinguette, C.P. Molecular electrocatalysts can mediate fast, selective CO₂ reduction in a flow cell. *Science* **2019**, *365*, 367–369. [[CrossRef](#)]
11. Hsieh, Y.C.; Senanayake, S.D.; Zhang, Y.; Xu, W.Q.; Polyansky, D.E. Effect of chloride anions on the synthesis and enhanced catalytic activity of silver nanocoral electrodes for CO₂ electroreduction. *ACS Catal.* **2015**, *5*, 5349–5356. [[CrossRef](#)]
12. Gu, J.; Hsu, C.S.; Bai, L.C.; Chen, H.M.; Hu, X.L. Atomically dispersed Fe³⁺ sites catalyze efficient CO₂ electroreduction to CO. *Science* **2019**, *364*, 1091–1094. [[CrossRef](#)] [[PubMed](#)]
13. Zhang, X.; Wang, Y.; Gu, M.; Wang, M.Y.; Zhang, Z.S.; Pan, W.Y.; Jiang, Z.; Zheng, H.Z.; Lucero, M.; Wang, H.L.; et al. Molecular engineering of dispersed nickel phthalocyanines on carbon nanotubes for selective CO₂ reduction. *Nat. Energy* **2020**, *5*, 684–692. [[CrossRef](#)]
14. Sun, X.H.; Tuo, Y.X.; Ye, C.L.; Chen, C.; Lu, Q.; Li, G.N.; Jiang, P.; Chen, S.H.; Zhu, P.; Ma, M.; et al. Phosphorus Induced electron localization of single Iron sites for boosted CO₂ electroreduction reaction. *Angew. Chem. Int. Ed.* **2021**, *60*, 23614–23618. [[CrossRef](#)] [[PubMed](#)]
15. Wang, J.J.; Wang, G.J.; Zhang, J.F.; Wang, Y.D.; Wu, H.; Zheng, X.R.; Ding, J.; Han, X.P.; Deng, Y.D.; Hu, W.B. Inversely tuning the CO₂ electroreduction and hydrogen evolution activity on metal oxide via heteroatom doping. *Angew. Chem. Int. Ed.* **2021**, *60*, 7602–7606. [[CrossRef](#)]
16. Hori, Y. Electrochemical CO₂ Reduction on Metal Electrodes. In *Modern Aspects of Electrochemistry*; Vayenas, C.G., White, R.E., Gamboa-Aldeco, M.E., Eds.; Springer: New York, NY, USA, 2008; pp. 89–189.
17. Hatsukade, T.; Kuhl, K.P.; Cave, E.R.; Abram, D.N.; Jaramillo, T.F. Insights into the electrocatalytic reduction of CO₂ on metallic silver surfaces. *Phys. Chem. Chem. Phys.* **2014**, *16*, 13814–13819. [[CrossRef](#)]
18. Benson, E.E.; Sampson, M.D.; Grice, K.A.; Smieja, J.M.; Froehlich, J.D.; Friebel, D.; Keith, J.A.; Carter, E.A.; Nilsson, A.; Kubiak, C.P. The electronic states of rhenium bipyridyl electrocatalysts for CO₂ reduction as revealed by X-ray absorption spectroscopy and computational quantum chemistry. *Angew. Chem. Int. Ed.* **2013**, *52*, 4841–4844. [[CrossRef](#)]
19. Lu, Q.; Rosen, J.; Zhou, Y.; Hutchings, G.S.; Kimmel, Y.C.; Chen, J.G.G.; Jiao, F. A selective and efficient electrocatalyst for carbon dioxide reduction. *Nat. Commun.* **2014**, *5*, 3242. [[CrossRef](#)]
20. Ma, M.; Trzesniewski, B.J.; Xie, J.; Smith, W.A. Selective and efficient reduction of carbon dioxide to carbon monoxide on oxide-derived nanostructured silver electrocatalysts. *Angew. Chem. Int. Ed.* **2016**, *55*, 9748–9752. [[CrossRef](#)]
21. Qiu, W.B.; Liang, R.P.; Luo, Y.L.; Cui, G.W.; Qiu, J.D.; Sun, X.P. A Br[−] anion adsorbed porous Ag nanowire film: In situ electrochemical preparation and application toward efficient CO₂ electroreduction to CO with high selectivity. *Inorg. Chem. Front.* **2018**, *5*, 2238–2241. [[CrossRef](#)]
22. Peng, X.; Karakalos, S.G.; Mustain, W.E. Preferentially oriented Ag nanocrystals with extremely high activity and faradaic efficiency for CO₂ electrochemical reduction to CO. *ACS Appl. Mater. Interfaces* **2018**, *10*, 1734–1742. [[CrossRef](#)]
23. Liu, S.Q.; Wu, S.W.; Gao, M.R.; Li, M.S.; Fu, X.Z.; Luo, J.L. Hollow porous Ag spherical catalysts for highly efficient and selective electrocatalytic reduction of CO₂ to CO. *ACS Sustain. Chem. Eng.* **2019**, *7*, 14443–14450. [[CrossRef](#)]
24. Ma, M.; Liu, K.; Shen, J.; Kas, R.; Smith, W.A. In situ fabrication and reactivation of highly selective and stable Ag catalysts for electrochemical CO₂ conversion. *ACS Energy Lett.* **2018**, *3*, 1301–1306. [[CrossRef](#)] [[PubMed](#)]
25. Zhang, Y.; Ji, L.; Qiu, W.B.; Shi, X.F.; Asiri, A.M.; Sun, X.P. Iodide-derived nanostructured silver promotes selective and efficient carbon dioxide conversion into carbon monoxide. *Chem. Commun.* **2018**, *54*, 2666–2669. [[CrossRef](#)] [[PubMed](#)]
26. Burdyny, T.; Smith, W.A. CO₂ reduction on gas-diffusion electrodes and why catalytic performance must be assessed at commercially-relevant conditions. *Energy Environ. Sci.* **2019**, *12*, 1442–1453. [[CrossRef](#)]
27. Zhang, X.; Li, J.C.; Li, Y.Y.; Jung, Y.H.; Kuang, Y.; Zhu, G.Z.; Liang, Y.Y.; Dai, H.J. Selective and high current CO₂ electro-reduction to multicarbon products in near-neutral KCl electrolytes. *J. Am. Chem. Soc.* **2021**, *143*, 3245–3255. [[CrossRef](#)] [[PubMed](#)]
28. Singh, M.R.; Goodpaster, J.D.; Weber, A.Z.; Head-Gordon, M.; Bell, A.T. Mechanistic insights into electrochemical reduction of CO₂ over Ag using density functional theory and transport models. *Proc. Natl. Acad. Sci. USA* **2017**, *114*, E8812–E8821. [[CrossRef](#)]
29. Weekes, D.M.; Salvatore, D.A.; Reyes, A.; Huang, A.X.; Berlinguette, C.P. Electrolytic CO₂ reduction in a flow cell. *Acc. Chem. Res.* **2018**, *51*, 910–918. [[CrossRef](#)]
30. Rabiee, H.; Ge, L.; Zhang, X.Q.; Hu, S.H.; Li, M.R.; Yuan, Z.G. Gas diffusion electrodes (GDEs) for electrochemical reduction of carbon dioxide, carbon monoxide, and dinitrogen to value-added products: A review. *Energy Environ. Sci.* **2021**, *14*, 1959–2008. [[CrossRef](#)]

31. De Arquer, F.P.G.; Dinh, C.T.; Ozden, A.; Wicks, J.; McCallum, C.; Kirmani, A.R.; Nam, D.H.; Gabardo, C.; Seifitokaldani, A.; Wang, X.; et al. CO₂ electrolysis to multicarbon products at activities greater than 1 A cm⁻². *Science* **2020**, *367*, 661–666. [[CrossRef](#)]
32. Dinh, C.T.; de Arquer, F.P.G.; Sinton, D.; Sargent, E.H. High rate, selective, and stable electroreduction of CO₂ to CO in basic and neutral media. *ACS Energy Lett.* **2018**, *3*, 2835–2840. [[CrossRef](#)]
33. Leonard, M.E.; Clarke, L.E.; Forner-Cuenca, A.; Brown, S.M.; Brushett, F.R. Investigating electrode flooding in a flowing electrolyte, gas-fed carbon dioxide electrolyzer. *ChemSusChem* **2020**, *13*, 400–411. [[CrossRef](#)] [[PubMed](#)]
34. Kas, R.; Hummadi, K.K.; Kortlever, R.; de Wit, P.; Milbrat, A.; Luiten-Olieman, M.W.J.; Benes, N.E.; Koper, M.T.M.; Mul, G. Three-dimensional porous hollow fibre copper electrodes for efficient and high-rate electrochemical carbon dioxide reduction. *Nat. Commun.* **2016**, *7*, 10748. [[CrossRef](#)] [[PubMed](#)]
35. Zhu, C.; Shen, G.F.; Chen, W.; Dong, X.; Li, G.H.; Song, Y.F.; Wei, W.; Sun, Y.H. Copper hollow fiber electrode for efficient CO₂ electroreduction. *J. Power Sources* **2021**, *495*, 229814. [[CrossRef](#)]
36. Rabiee, H.; Zhang, X.Q.; Ge, L.; Hu, S.H.; Li, M.R.; Smart, S.; Zhu, Z.H.; Yuan, Z.G. Tuning the product selectivity of the Cu hollow fiber gas diffusion electrode for efficient CO₂ reduction to formate by controlled surface Sn electrodeposition. *ACS Appl. Mater. Interfaces* **2020**, *12*, 21670–21681. [[CrossRef](#)]
37. Rabiee, H.; Ge, L.; Zhang, X.Q.; Hu, S.H.; Li, M.R.; Smart, S.; Zhu, Z.H.; Yuan, Z.G. Shape-tuned electrodeposition of bismuth-based nanosheets on flow-through hollow fiber gas diffusion electrode for high-efficiency CO₂ reduction to formate. *Appl. Catal. B-Environ.* **2021**, *286*, 119945. [[CrossRef](#)]
38. Dinh, C.T.; Burdyny, T.; Kibria, M.G.; Seifitokaldani, A.; Gabardo, C.M.; de Arquer, F.P.G.; Kiani, A.; Edwards, J.P.; De Luna, P.; Bushuyev, O.S.; et al. CO₂ electroreduction to ethylene via hydroxide-mediated copper catalysis at an abrupt interface. *Science* **2018**, *360*, 783–787. [[CrossRef](#)]
39. Liu, S.B.; Tao, H.B.; Zeng, L.; Liu, Q.; Xu, Z.G.; Liu, Q.X.; Luo, J.L. Shape-dependent electrocatalytic reduction of CO₂ to CO on triangular silver nanoplates. *J. Am. Chem. Soc.* **2017**, *139*, 2160–2163. [[CrossRef](#)]
40. Deng, W.Y.; Zhang, L.; Dong, H.; Chang, X.X.; Wang, T.; Gong, J.L. Achieving convenient CO₂ electroreduction and photovoltage in tandem using potential-insensitive disordered Ag nanoparticles. *Chem. Sci.* **2018**, *9*, 6599–6604. [[CrossRef](#)]
41. Dutta, A.; Morstein, C.E.; Rahaman, M.; Lopez, A.C.; Broekmann, P. Beyond copper in CO₂ electrolysis: Effective hydrocarbon production on silver-nanofoam catalysts. *ACS Catal.* **2018**, *8*, 8357–8368. [[CrossRef](#)]
42. Fu, H.Q.; Zhang, L.; Zheng, L.; Liu, P.F.; Zhao, H.J.; Yang, H.G. Enhanced CO₂ electroreduction performance over Cl⁻ modified metal catalysts. *J. Mater. Chem. A* **2019**, *7*, 12420–12425. [[CrossRef](#)]
43. Kim, C.; Jeon, H.S.; Eom, T.; Jee, M.S.; Kim, H.; Friend, C.M.; Min, B.K.; Hwang, Y.J. Achieving selective and efficient electrocatalytic activity for CO₂ reduction using immobilized silver nanoparticles. *J. Am. Chem. Soc.* **2015**, *137*, 13844–13850. [[CrossRef](#)] [[PubMed](#)]
44. Jiang, K.; Kharel, P.; Peng, Y.; Gangishetty, M.K.; Lin, H.-Y.G.; Stavitski, E.; Attenkofer, K.; Wang, H. Silver nanoparticles with surface-bonded oxygen for highly selective CO₂ reduction. *ACS Sustainable Chem. Eng.* **2017**, *5*, 8529–8534. [[CrossRef](#)]
45. Hsieh, Y.C.; Betancourt, L.E.; Senanayake, S.D.; Hu, E.Y.; Zhang, Y.; Xu, W.Q.; Polyansky, D.E. Modification of CO₂ reduction activity of nanostructured silver electrocatalysts by surface halide anions. *ACS Appl. Energy Mater.* **2019**, *2*, 102–109. [[CrossRef](#)]
46. Lee, C.Y.; Zhao, Y.; Wang, C.Y.; Mitchell, D.R.G.; Wallace, G.G. Rapid formation of self-organised Ag nanosheets with high efficiency and selectivity in CO₂ electroreduction to CO. *Sustain. Energy Fuels* **2017**, *1*, 1023–1027. [[CrossRef](#)]
47. Ma, S.C.; Lan, Y.C.; Perez, G.M.J.; Moniri, S.; Kenis, P.J.A. Silver supported on titania as an active catalyst for electrochemical carbon dioxide reduction. *ChemSusChem* **2014**, *7*, 866–874. [[CrossRef](#)]
48. Rosen, J.; Hutchings, G.S.; Lu, Q.; Rivera, S.; Zhou, Y.; Vlachos, D.G.; Jiao, F. Mechanistic insights into the electrochemical reduction of CO₂ to CO on nanostructured Ag surfaces. *ACS Catal.* **2015**, *5*, 4293–4299. [[CrossRef](#)]
49. Dunwell, M.; Luc, W.; Yan, Y.S.; Jiao, F.; Xu, B.J. Understanding surface-mediated electrochemical reactions: CO₂ reduction and beyond. *ACS Catal.* **2018**, *8*, 8121–8129. [[CrossRef](#)]
50. Liu, M.; Pang, Y.J.; Zhang, B.; De Luna, P.; Voznyy, O.; Xu, J.X.; Zheng, X.L.; Dinh, C.T.; Fan, F.J.; Cao, C.H.; et al. Enhanced electrocatalytic CO₂ reduction via field-induced reagent concentration. *Nature* **2016**, *537*, 382–386. [[CrossRef](#)]